

## Dynamic Modeling for 20 kWe Heat Pipe Fission Battery with Dual Power Conversion System

Kyeong Jun Park, Tae Hwan Kim, Hee Sang Yoo, Young Beom Jo\* and Eung Soo Kim\*

Department of Nuclear Engineering, Seoul National University

\*Corresponding author: kes7741@snu.ac.kr, paul406@snu.ac.kr

### 1. Introduction

The micro-nuclear reactor, known as the heat pipe nuclear fission battery, offers a portable and dependable energy solution for remote locations, functioning independently of the primary power grid [1]. Consisting of a solid core, heat pipe (HP) elements, and thermoelectric generators (TEG), this reactor system ensures both stability and mobility, resembling the operation of a DC battery due to its lack of moving parts [2].

While research focusing on individual components of nuclear fission batteries has been active, investigations into system-level transients, dynamic behavior, and thermal interactions among components have been relatively limited. To bridge this gap, a previous study by J.S. Chi (2023) developed a fission battery system model with a 10kWe output for an underwater vehicle as a benchmark design, conducting steady-state and dynamic simulations using AMESim Software [3]. The findings validated the feasibility and stability of the 10kWe fission battery system with a 15% efficiency.

Nevertheless, the prior research's model, although stable, exhibited an efficiency constraint attributed to the utilization of a static power conversion system—the thermoelectric generator (TEG). This study enhances the previously proposed Micro Heat Pipe Fission Battery model, elevating efficiency from 15% to achieve a stable and efficient system, while confirming its durability. To achieve this, a high-efficiency dynamic power conversion system, the Free-Piston Stirling Generator (FPSG), is modeled using a non-linear analysis approach to capture its physical characteristics. This model is then integrated with the TEG model from the previous study, forming a stable and efficient dual power conversion system.

### 2. The 10kWe Heat Pipe Fission Battery

The study from Seoul National University introduces a 10 kWe heat pipe fission battery system for underwater use, featuring a reactor core, heat pipes, and a TEG, detailed in Figure 1 and Table I [4]. Designed for a thermal output of 74 kWt, it uses 11% enriched UN fuel and a sodium heat pipe mechanism chosen for its temperature range. The system's core layout uses 37 sodium heat pipes and 90 fuel rods in a triangular array to analyze core behavior and its influence on battery power, applying point kinetic equations and reactivity feedback.

The dynamic model of the 10 kWe heat pipe fission battery was developed in AMESim (Advanced Modeling

Environment for Simulation), a versatile software for system-level multi-domain simulation that facilitates the modeling and analysis of intricate engineering systems.

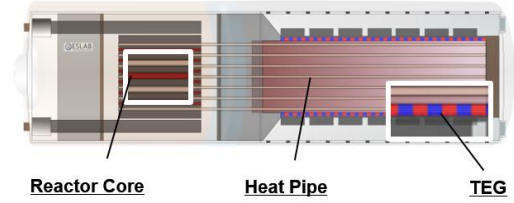


Fig 1. 10kWe Heat Pipe Nuclear Fission Battery

Table I. Design Specifications for 10 kWe Micro Fission Battery

Parameters	Value	Unit
Number of Layers	4	-
Fuel Material	UN	
Matrix (Moderator) Material	Zr2H3	
Enrichment	11	%
Core Diameter	40	cm
Height of Active Core Zone	40	cm
Heat Pipe Material	Sodium	-
TEG Material	PbTe	
Number of TE Elements	12347	EA
Thermal Power	74	kWt
Electric Power	11.3	kWe
Efficiency	15.3	%

#### 2.1 The Core

The core in the previous research was modeled as an equivalent annulus for thermal energy conservation, divided into fuel, heat pipe, and core matrix zones with 11 axial nodes each. The fuel section was further segmented radially into five columns to address heat from fission reactions. The dynamic heat equation for each component  $i$  within the core area is as follows:  $M$ ,  $C_p$ , and  $T$  denote the mass, heat capacity, and temperature of each component respectively, while  $R$  and  $Q$  represent thermal resistance and heat generation, respectively.

$$M_i C_{pi} \frac{dT_i}{dt} = \sum_j \frac{T_j - T_i}{R_{ij}} + \dot{Q}_i \quad (1)$$

#### 2.2 The Heat Pipe

A heat pipe functions by exploiting the working fluid's phase change, modeled around thermal resistance and considering sonic, entrainment, boiling, viscous, and capillary operational limits [5]. It is divided into evaporative and condensation areas, each with three nodes (wall, wick, chamber), with node-specific resistances detailed in Table II. The essential heat

transfer equation governing the process is succinctly formulated as follows.

$$M_i C_{pi} \frac{dT_i}{dt} = \sum_j \frac{T_j - T_i}{R_{ij}}. \quad (2)$$

Table II. Node-specific resistances

	$R_{ij}$ [K/W]
Evap. Shell – Wick	$R_{23} = \frac{1}{2\pi r_i L_e} \left[ \frac{r_o - r_i}{2k_s} + \frac{r_i - r_w}{2k_l} \right]$
Evap. Wick – Chamber	$R_{34} = \frac{1}{2\pi r_w L_e} \left[ \frac{r_i - r_w}{2k_{l,eff}} \right]$
Cond. Chamber – Wick	$R_{56} = \frac{1}{2\pi r_w L_e} \left[ \frac{r_i - r_w}{2k_{l,eff}} \right]$
Cond. Wick – Shell	$R_{67} = \frac{1}{2\pi r_i L_e} \left[ \frac{r_o - r_i}{2k_s} + \frac{r_i - r_w}{2k_{l,eff}} \right]$

### 2.3 The TEG

The TEG's modeling involved merging a thermal energy conservation equation with the Thomson and Seebeck effects [6]. Heat transfer within a thermoelectric element is described in Equation (3), which includes the Joule heating caused by the flow of electric. Within this equation,  $j$ ,  $\rho$ , and  $V$  stand for the current, density, and volume, respectively.

$$M_i C_{pi} \frac{dT_i}{dt} = \sum_j \frac{T_j - T_i}{R_{ij}} + j_i^2 \rho_i V_i \quad (3)$$

The difference in heat absorbed at the hot junction and expelled at the cold junction determines the power output of the TEG, as defined by equation (4) with the thermoelectric effect accounted for [6]. Equation (5) specifies the conversion efficiency, where  $Z\bar{T}$  represents the dimensionless figure of merit, essential for assessing thermoelectric materials. This TEG model comprehensively computes the heat movement across the thermoelectric (TE) element, the production of thermoelectric power, and the efficiency of these processes.

$$\dot{W}_n = \dot{Q}_h - \dot{Q}_c = n[\alpha I(T_h - T_c) - I^2 R] = nI^2 R_L \quad (4)$$

$$\eta_{th} = \frac{\left(1 - \frac{T_c}{T_h}\right) \frac{R_L}{R}}{\left(1 - \frac{R_L}{R}\right) - \frac{1}{2} \left(1 - \frac{T_c}{T_h}\right) + \frac{1}{2Z\bar{T}} \left(1 - \frac{R_L}{R}\right)^2 \left(1 + \frac{T_c}{T_h}\right)} \quad (5)$$

### 2.4 The Reactivity Feedback

The model developed incorporates the effect of reactivity feedback, calculating reactivity through equation (6) with considerations for the Fuel Temperature Coefficient (FTC) and Moderator Temperature Coefficient (MTC). This calculation is integrated with Point Kinetics Equations (PKE) (7) and (8) to evaluate neutron flux [7], subsequently influencing the core temperature via the heat generated from fission as a result of changes in neutron flux within the specified core design. The symbols  $\alpha_{T_f}$ ,  $\alpha_{T_m}$ ,  $\rho$ ,  $T_f(t)$ ,  $T_m(t)$ ,  $N$ ,  $\Lambda$ ,  $\beta$ ,  $\lambda$ , and  $C_i(t)$  denote the fuel temperature coefficient, moderator temperature coefficient,

reactivity, average fuel temperature, average moderator temperature, neutron flux, neutron average generation time, fraction of delayed neutrons, decay constant, and precursor neutron density, respectively.

$$\rho(t) = \rho_0 + \alpha_{T_f}(T_f(t) - T_{f_0}) + \alpha_{T_m}(T_m(t) - T_{m_0}) + \delta\rho_{ext}(t) \quad (6)$$

$$\frac{dN(t)}{dt} = \frac{\rho(t) - \beta}{\Lambda(t)} N(t) + \sum_i \lambda_i C_i(t) \quad (7)$$

$$\frac{dC_i(t)}{dt} = \frac{\beta_i}{\Lambda(t)} N(t) - \lambda_i C_i(t) \quad (8)$$

## 3. Development of the Dynamic FPSG Model

The FPSG's has been advanced from the traditional Stirling cycle through the elimination of mechanical drive components and the introduction of a free piston system, enhancing its power via pressurization. This generator stands out for its exceptional efficiency, reliability, compactness, and long lifespan, sparking considerable research interest [8]. As shown in figure 2, it features two independent pistons in a single cylinder, connected to springs, performing reciprocating movements in different cells, with efficiency improved by a regenerator and a permanent magnet around the power piston. Electrical energy is generated through the reciprocating motion of the pistons, facilitated by a linear alternator [9, 10]. The FPSG operates on a cycle of two isochoric and two isothermal processes, ideally optimized by a 90-degree phase difference between the displacer and power pistons for effective heating and cooling [11].

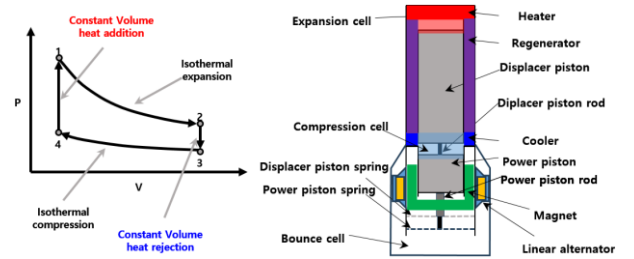


Fig 2. The thermodynamic cycle and components of FPSG

### 3.1 Methodology

The analysis of Free-Piston Stirling Engines (FPSEs) requires merging thermodynamic and dynamic principles due to their intricate dynamics [12]. This field of study is segmented into linear analyses, which simplify fluid and piston dynamics, and nonlinear analyses that provide detailed insights into complex behaviors within the engine [13]. A nonlinear approach is utilized in this research for accurate FPSE modeling, incorporating a simplified model for the alternator system and electrical circuits [14]. Assumptions such as no working fluid leakage, ideal gas behavior of the working fluid, uniform pressure gradients at each cell, adiabatic cylinder walls, linear temperature changes between cells, and constant heater and cooler temperatures guide the modeling process. Specific

equations for each domain ensure a comprehensive depiction of the processes involved, including heating, cooling, piston motion, and electricity generation.

### 3.1.1 The thermal and fluidic domain

By applying the fundamental equations (9) rooted in energy conservation principles, the variations in mass and temperature across each cell are calculated using the initial values designated to each cell.

$$\frac{dU}{dt} = \sum \dot{m}_i h_i + \frac{dQ}{dt} + \frac{dW}{dt} \quad (9)$$

( $U$  : the internal energy,  $\dot{m}_i$  : the mass flow rate of the cell  $i$ ,  $h_i$  : the specific enthalpy of the cell  $i$ ,  $Q$  : the heat,  $W$  : the work of the pressure forces)

The variations of the mass and temperature of each cell and the assumption about temperature are applied to calculate the pressure and volume variations with the piston mechanical domain to implement behavior of FPSE and finally gain the current and voltage by the piston movement.

### 3.1.2 The piston mechanical domain

Within the mechanical domain of the piston, the force applied to the piston, which takes into account variations in pressure and the generated electromotive force, is determined using the fundamental equation of motion ( $F=ma$ ). This computation facilitates the estimation of both the piston's position and its velocity.

The equation of the displacer piston is [15]:

$$M_d \ddot{x}_d + c_d \dot{x}_d + K_d x_d = F_d \quad (10)$$

where  $M_d$  is the displacer piston mass.  $x_d$  is the displacer piston displacement.  $c_d$  is the displacer piston damping coefficient.  $K_d$  is the spring constant.  $F_d$  is the pressure force between the expansion and compression cell.

The equations of the power piston can be obtained [15]:

$$M_p \ddot{x}_p + c_p \dot{x}_p + K_p x_p = F_p + F_e \quad (11)$$

$$F_e = N \frac{d\phi}{dx_p} \eta_{mag} I_{alt} = BLI_{alt} = K_i I_{alt} \quad (12)$$

where  $M_p$  is the power piston mass ( $kg$ ).  $x_p$  is the power piston displacement ( $m$ ).  $c_p$  is the power piston damping coefficient ( $N \cdot s/m$ ).  $K_p$  is the spring constant ( $N/m$ ).  $F_p$  is the pressure force between the compression and bounce cell.  $B$  is the magnetic induction intensity of the linear generator ( $T$ ).  $L$  is the coil length ( $m$ ).  $N$  is number of turns of the generator winding.  $\phi$  is the magnetic flux ( $Wb$ ).  $\eta_{mag}$  is generator magnetic efficiency.  $I_{alt}$  is generator current ( $A$ ).  $K_i$  : alternator current electromagnetic force constant ( $N/A$ ).

### 3.1.3 The electrical domain

The coils are considered strongly coupled to the magnets, so the electromotive force  $v_{emf}$  and the current  $I_{alt}$  can be calculated as follow [15]:

$$v_{emf} = K_e \cdot \dot{x}_p, \text{ where } K_e = N \frac{d\phi}{dx_p} \quad (13)$$

$$v_{emf} = v_{R_{alt}} + v_{L_{alt}} + v_{C_t} + v_{R_{load}} \quad (14)$$

$$\frac{dI_{alt}}{dt} = \frac{K_e}{L_{alt}} \dot{x}_p - \frac{R_{alt} + R_{load}}{L_{alt}} I_{alt} - \frac{1}{L_{alt}} v_{C_t} \quad (15)$$

$$\frac{dv_{C_t}}{dt} = \frac{1}{C_t} I_{alt} \quad (16)$$

where  $K_e$  is the alternator constant ( $V \cdot s/m$ ).  $L_{alt}$  is the generator inductance (H).  $R_{alt}$  is the generator resistance ( $\Omega$ ).  $R_{load}$  is the external load resistance ( $\Omega$ ).  $C_t$  is the tuning capacitance ( $\mu F$ ).

The relationship between inductance and the capacitance to form resonant frequency with the engine is as follows [16]:

$$\frac{1}{2\pi\sqrt{L_{alt}C_t}} = f \quad (17)$$

### 3.2 The input parameters and simulation results

Figure 3 displays the AMESim model of the FPSG and its simulation outcomes, while Table III enumerates the input parameters utilized in crafting the FPSG model. The input data is established by drawing on the specifications of NASA's Re-1000 FPSE [17].

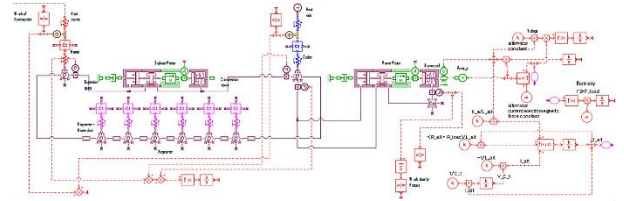


Fig 3. The FPSG model using AMESim

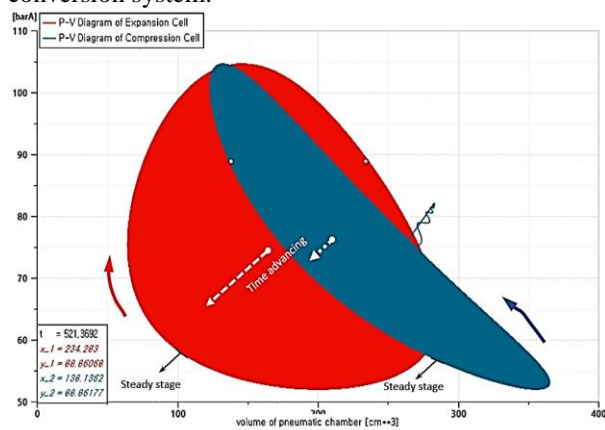
Table III. The input parameters for FPSG

Parameters	Value	Unit
FPSG type	γ	-
Working gas	Helium	-
Cylinder material	SUS	-
Displacer piston (D.P.) mass	0.426	kg
Power piston (P.P.) mass	7.9	kg
D.P. diameter	56.7	mm
D.P. rod diameter	16.6	mm
P.P. diameter	57.5	mm
P.P. rod diameter	16.6	mm
D.P., P.P. seal clearance	0.033	mm
D.P. spring stiffness	20	N/mm
P.P. spring stiffness	250	N/mm
Expansion & Heater cell volume	0.08	L
Regenerator volume	0.13	L
Compression & Cooler cell volume	0.08	L
Bounce cell volume	5	L
Coil Resistance	0.5	Ω
external load Resistance	20	Ω
Transduction coefficient	65	N/A

The FPSG system attained a stable oscillatory state from the heat provided by the source and sink, bypassing the need for explicit ignition conditions. Temperature equilibrium was reached across the expansion, regenerator, and compression cells, facilitating synchronized piston movement and effective heat exchange. A notable pressure differential was maintained across the power piston to ensure efficient mechanical work, with compression and bounce cell pressures recorded between 53.63 to 102.9 bar and 72.46 to 80.33 bar, respectively. Operating parameters included displacer and power piston amplitudes of 4.52 cm and 5.505 cm, respectively, engine and generator frequency at 34.48 Hz. This configuration allowed the system to convert a thermal input of 42.93 kW into an electrical output of 14.85 kW, demonstrating a 34.59% efficiency.

### 3.3 Validation of the FPSG model

The FPSG's modeling validation was verified by analyzing some of its characteristics. A 49.65-degree phase difference between the displacer and power pistons was observed, against the ideal 90 degrees and the NASA Stirling engines' 57.5(RE-1000) and 67(CTPC) degrees phase differences [17]. Also the P-V diagrams in Figure 4 depict the transition from small ellipses to maximal paths in opposite directions upon reaching steady oscillation, indicating efficient energy conversion to 14.85 kWe. The alignment of engine and generator frequencies was also confirmed. This comprehensive evaluation validates the FPSG model, setting the stage for further modeling of the dual power conversion system.



The inner areas of each diagram mean the Work done by pistons

$$W_{Piston} = \int_0^t (P_E \frac{dv_E}{dt} + P_C \frac{dv_C}{dt}) dt$$

Fig 4. The P-V diagram of expansion & compression cell of FPSG

## 4. Development of Dynamic Simulation Model for 20 kWe Micro Heat Pipe Fission Battery with Dual Power Conversion System

### 4.1 Integration of the entire models of the system

The dualization of the static TEG and dynamic FPSG power conversion systems utilizes the established 74 kWth solid-core model from prior research (J.S. Chi, 2023), employing the McCARD methodology [18]. When tuning the electrical output to match the core's power, FPSG's dynamic properties are factored in, leading to adjustments being made primarily to the TEG due to its simpler input power modulation and the possibility for redesign. The input power for the FPSG is set at 43 kWt, prompting a corresponding adjustment of the TEG's input power to 31 kWt. For the dual power conversion system to align with the designated core power, TEG parameters were reevaluated using the EES(Engineering Equation Solver) model from previous TEG research [4], with these revised parameters incorporated into the AMESim TEG model.

The previously implemented core, heat pipes, and neutronics models have been integrated with the dual power conversion system into a unified system through AMESim, as shown in Figure 5. This integration takes into account the whole system geometry and incorporates a heat distributor made of 100kg of copper (Cu). Employing copper for heat distribution facilitates the effective movement of thermal energy from the heat pipes to both the heater head of the FPSG and the high-temperature area of the TEG.

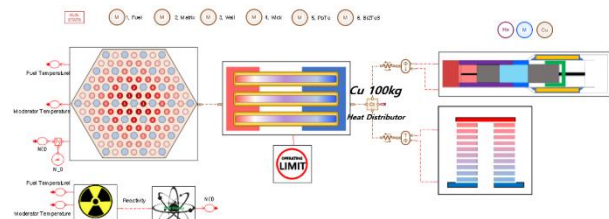


Fig 5. The 20 kWe Heat pipe Fission Battery using AMESim

### 4.2 Simulation results

The 20 kW Micro Heat Pipe Fission Battery, equipped with a Dual Power Conversion System, achieves a stable condition roughly 1,000 seconds post-startup, as demonstrated by the simulation outcomes. Figure 6 graphs highlight the dynamics of crucial variables, showing that both the core temperature and neutron flux initially reach elevated levels, contributing to significant power generation from the core until the FPSG stabilizes into an oscillatory pattern. As the system nears a steady state, reactivity steadily zeroes out, and neutron flux stabilizes at 1.058, marking the effective attainment of steady state across the system.

Simulation outcomes for the system under normal conditions, detailed in Tables IV, reveal minor discrepancies from the anticipated metrics for key components prior to their integration. Initially, there's a 3.2% reduction in core power to 71.62 kW. However, due to FPSG's high efficiency, the system's total power output surges by 86.2% over past research models to 21.05 kW, with an efficiency boost of 92% over the baseline to 29.39%. While core and heat pipe alterations

remain slight, the TEG's high-temperature segment experiences a 2.7% decrease, and its low-temperature segment a 10.4% increase against the baseline. In this study's dual power conversion system, the TEG's assigned input power, initially 31 kW, adjusts to 26.64 kW, marking a 12.6% decrease. Following TEG parameter adjustments, its efficiency jumps by 16.4% to 17.81%, exceeding expectations. FPSG simulation findings also diverge slightly from predicted values. Relative to the standalone modeled input power for FPSG, the allocated input power increases by 4.6%, while the high-temperature segment's temperature drops by 1.3%. The pistons' amplitude sees a 3.1% rise from the individual model, leading to about a 10% hike in electrical output and a 5% improvement in efficiency.

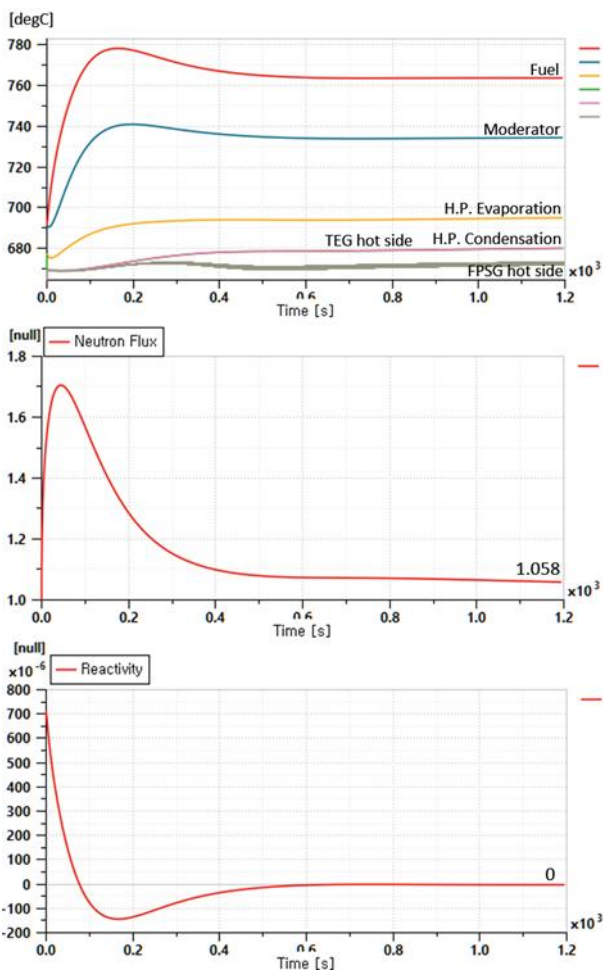


Fig 6. Behavior of key variables of the System

Table IV.

Variables	Value	Unit
Reactor Thermal Power	71.62(3.2%↓)	kWt
Entire Electric Power	21.05(86.2%↑)	kWe
Efficiency	29.39(92.1%↑)	%
TEG Hot Side Temperature	924.7(2.7%↓)	K
TEG Cold Side Temperature	334.8(10.4%↑)	K
TEG Thermal Power Input	26.64(12.6%↓)	kWt
TEG Electric Power Output	4.74(-)	kWe
TEG Efficiency	17.81(16.4%↑)	%

Thermal Power Input	44.9(4.6%↑)	kWt
Heater Temperature	946.1 (1.3%↓)	K
D.P. Amplitude	4.66(3.1%↑)	cm
P.P. Amplitude	5.68(3.1%↑)	cm
Electric Power Output	16.31(9.8%↑)	kWe
Efficiency	36.26(4.8%↑)	%

## 5. Summary

Drawing upon existing research (Chi, 2023), this research crafted a dynamic simulation framework for a micro heat pipe fission battery system, integrating a core, heat pipe, and a dual power conversion mechanism encompassing TEG and FPSG. The FPSG's engine segment utilized a non-linear analysis method, and for the generator, a streamlined alternator system analysis model was adopted. These comprehensive models and equations were seamlessly integrated within the AMESim platform.

This model efficiently stabilized from an inactive state to a steady state without the need for predefined start-up conditions, achieving steady state within approximately 1,000 seconds under standard operating conditions. Implementing a dual power conversion system, which includes the highly efficient FPSG, led to an impressive enhancement in the battery's power output and efficiency by 86% and 92%, reaching 21.05 kWe and 29.39% respectively, surpassing the outcomes from prior research that solely utilized the static TEG system.

To sum up, this investigation demonstrates the development of an accessible and rapid analytical tool for examining the behaviors of fission batteries, integrating a sophisticated power conversion architecture. Furthermore, it provides the practicality of designing a nuclear fission battery featuring a dual power conversion system, offering insights for ongoing micro-reactor research advancements.

## REFERENCES

- [1] International Atomic Energy Agency, "Advances in Small Modular Reactor Technology Developments 2020 edition", [https:// aris.iaea.org/Publications/SMR\\_Book\\_2020.pdf](https://aris.iaea.org/Publications/SMR_Book_2020.pdf)
- [2] Testoni, Raffaella, Andrea Bersano, and Stefano Segantin. "Review of nuclear microreactors: Status, potentialities and challenges." *Progress in Nuclear Energy* 138 (2021): 103822.
- [3] J.S. Chi, et al. "Dynamic Simulation Model for 10 kWe Heat Pipe Nuclear Fission Battery" *Energy Reports* 2023, International Symposium on Zero-Carbon Energy Systems, 10–12 January 2023, Tokyo Institute of Technology, Japan
- [4] Park, S. S., Kim, J. W., Kim, Y. I., Kim, J. H., Chae, H., Chi, J. S., & Jo, Y. B. (2021). 10 kWe Heat Pipe Reactor Battery Design for Underwater Vehicles
- [5] Nemeč, P., Čaja, A., & Malcho, M. (2013). Mathematical model for heat transfer limitations of heat pipe. *Mathematical and Computer Modelling*,
- [6] Lee, H. (2016). *Thermoelectrics: design and materials*. John Wiley & Sons.
- [7] Petersen, C. Z., Dulla, S., Vilhena, M. T., & Ravetto, P. (2011). An analytical solution of the point kinetics equations

with time-variable reactivity by the decomposition method. *Progress in Nuclear Energy*, 53(8), 1091-1094.

[8] Thombare, D.G.; Verma, S.K. Technological development in the Stirling cycle engines. *Renew. Sustain. Energy Rev.* 2008, 12, 1–38.

[9] Walker G. *Stirling Engines*. Oxford: Clarendon Press; 1980.

[10] Norman, S. *Control System Engineering*, 4th ed.; California State Polytechnic University: Pomona, CA, USA, 2004.

[11] Thombare, D.G.; Verma, S.K. Technological development in the Stirling cycle engines. *Renew. Sustain. Energy Rev.* 2008, 12, 1–38.

[12] Lewandowski, E.; Regan, T. Overview of the GRC Stirling Converter System Dynamic model. In *Proceedings of the 2nd International Energy Conversion Engineering Conference*, Providence, RI, USA, 16–19 August 2004

[13] Zare SH, Tavakolpour-Saleh AR. Nonlinear dynamic analysis of solar free piston hot-air engine. *Modares Mech Eng.* 2015;15(9): 223-234.

[14] Benvenuto, G., and F. De Monte. "Analysis of free-piston Stirling engine/linear alternator systems. Part I-Theory." *Journal of propulsion and power* 11.5 (1995): 1036-1046.

[15] Li, Huaqi, et al. "Development of a performance analysis model for free-piston stirling power convertor in space nuclear reactor power systems." *Energies* 15.3 (2022): 915.

[16] Jia, Zilong, et al. "Study on the coupling between engine and alternator in a free-piston Stirling generator." *Applied Thermal Engineering* 217 (2022): 119222.

[17] Schreiber, Jeffrey G., Steven M. Geng, and Gary V. Lorenz. "RE-1000 free-piston Stirling engine sensitivity test results." *National Aeronautics and Space Administration Report* (1986).

[18] Shim, H. J., Han, B. S., Jung, J. S., Park, H. J., & Kim, C. H. (2012). McCARD: Monte Carlo code for advanced reactor design and analysis. *Nuclear Engineering and Technology*, 44(2), 161-176.